Modelling and Analysis of Vibration on Power Electronic Module Structure and Application of Model Order Reduction

Pushpa Rajaguru, Hua Lu, Chris Bailey, and Martina Bella

Department of Mathematical Sciences, University of Greenwich, Faculty of Architecture, Computing and Humanities, University of Greenwich, London, SE10 9LS

Abstract— Modelling and analysis of vibration of an IGBT power electronic module (PEM) structure were undertaken. PEM structure considered in this study was without molding compound and wirebonds. The most critical resonant frequency was identified by modal analysis. At the critical frequency of 1345Hz, for the vertical displacement of the base excitation, subsequent stress distribution on the PEM structure was analysed. Concurrent vibration and thermo-mechanical fatigue loads on the reliability of PEM structure solder interconnects were also estimated by widely used linear damage superposition approach. It was concluded that the at critical resonant frequency the vibration induced damage is more severe than the thermo-mechanical fatigue loading. In addition, a quarter car model (QCM) was used to mimic the dynamic interaction between the rough road surface and an electric vehicle (EV) in order to analyse the road surface roughness induced excitation on the PEM structure in the engine compartment. Stress and strain distribution on the PEM structure due to road surface roughness were analysed. Furthermore, three Krylov subspace based model order reduction (MOR) techniques were applied to the resulting dynamic system in vibration analysis. Due to the limits on computing resources, a submodel was utilized for MOR analysis. Within the three MOR techniques, Passive Reduced order Interconnect Macromodeling Algorithm (PRIMA) MOR technique performs better than the other techniques. Computational time ratio between reduced system iteration and the full system iteration is 1:53.

I. INTRODUCTION

Power electronic modules are self-contained electronics components that are widely used in aerospace automotive and alternative energy generation. They play a vital part in conversion, control, alternative energy generation and distribution, see Sheng et al [1]. PEMs are highly inhomogeneous structures consists of semiconductor, ceramic, copper, aluminium, polymer, and sometimes composite materials as in Figure 1. These materials are assembled together in the packaging manufacturing process using soldering, direct bond copper (DBC), wirebond, and pressure contact interconnect techniques.
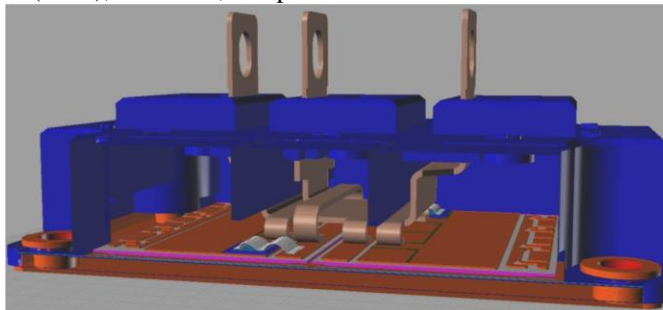

Figure 1: An IGBT power electronic module.

In automotive application, IGBT integrated into compact power modules are widely used as power switches in electric traction drives for electric vehicles (EVs) and hybrid electric vehicles (HEVs). In electric traction drive system, the battery cannot be connected directly to the electric motors, hence DC current from the battery must be modified to an AC supply and regulated in a suitable form to feed into the electric drive system. PEM is used for this purpose. The environment condition of EV and HEV are highly demanding in terms of ambient temperature, power and temperature cycling, hence PEM devices should operate in a harsh condition such as high junction temperature. Furthermore, power cycling introduces stresses at the interface materials such as bond wires, substrate, solder etc. Many studies have been reported for thermal and power cycling related failure mechanisms of PEM devices, see Durand et al [2]. Vibration and shock can also cause a failure mechanism in PEM devices, specifically in EV or HEV for a severe road profile. According to data (see Steinberg [3]) from the United States Air Force, the failure rate of electronic devices by vibration and shock related failures is approximately 20%, hence vibration is a significant failure mode in microelectronics. In severe road condition, PEM devices operate in vibrational mode on the suspension system which results in damage to wirebond and solder interconnect. If one of the interconnect structures is damaged, then the entire PEM device may fail due to a short circuit.

Gu et al [4] investigated the effect of vibration loading for electronic printed circuit board (PCB) and developed a physics of failure (PoF) based remaining useful life (RUL) estimation. An analytical model combined with finite element analysis and sensory data were utilised to predict the stresses at the solder interconnect of the PCB board. The RUL was approximated using a cumulative damage fatigue model combined with a cycle counting algorithm and then validated with experimental data. Park et al [5] proposed a structural design methodology for evaluating the mechanical safety condition of the solder joint of plastic ball grid array (PBGA) assembly under random vibration loading for spaceborne electronics. Jiang et al [6] proposed a failure characterization of quad flat package (QFP) structure under random vibration loading and identified four modes of failure on the QFP structure. Another finite element vibration analysis on PCB package with ball grid array (BGA) solder joints was investigated by Liu et al [7], and the results conclude that greater amplitude random vibration loading results in shorter fatigue life of BGA joints. A similar study by An [8] et al, investigated the effect of combined loading of temperature and vibration on PCB assembly with PBGA solder joints.

A huge number of research literature dedicated to electronic package interconnect vibration modelling, analysis, and testing, however modelling vibration analysis in the context of PEM structure has not been adequately addressed in the literature, which is the main focus on this study. Due to limited academic computing resources, we focused on solder interconnect failure. Moreover, in order to minimize the computational complexity, an application of model order reduction to the resulting time invariant system in PEM device vibration analysis is also gently addressed.

II. MODELLING VIBRATION OF PEM

The IGBT PEM device used in this study is as in Figure *2*. To reduce the modelling complexity due to limited academic computing resources, the epoxy molding compound (EMC) and wirebond were removed in the model as in Figure 2. In the PEM structure, copper busbar serves as electric terminals.
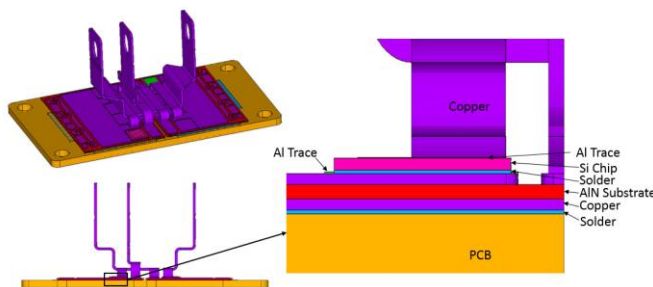

Figure 2: PEM device structure without molding compound (encapsulation)

The model consists of sandwiched layers of copper/ceramic substrate/copper, chip, aluminum trace, solder interconnect, and a baseplate (PCB). The common baseplate material is alumina (aluminium oxide) with direct copper bonding (DCB). This is replaced with aluminium nitride when improved thermal conductivity is required. Copper is generally used for the base plate material due to its good electrical and thermal properties. The copper base plate has a reasonable temperature cycling capability, however, for applications requiring extended temperature cycling capabilities an automotive base plate made from aluminium silicon carbide (AlSiC) metal matrix composite (MMC) is used because it has a good CTE match between the substrate and the base plate thus minimizing thermo-mechanical stresses. AlSiC does not have as good thermal conductivity as the copper but when used with aluminium-nitride substrate adequate overall thermal resistance is obtained. The material properties used in the model is as in Table 1.

Table 1: Material Properties of the PEM structure

Material	Density (Kg/m^3)	Young's Modulus (GPa)	Poisson Ratio	Coefficient of Thermal Expansion (10^{-6}/°C)
Aluminum Trace (Al)	2700	70.6	0.345	24.5
Copper (Cu)	8960	110	0.35	17
Substrate (AlN)	3260	310	0.24	5.6
Solder (Sn3.5Ag)	7360	54.05-0.193×T(°C)	0.4	21.85-0.0239×T(°C)
Si chip	2329	170	0.28	2.6
PCB (AlSiC) [9]	3000	200	0.3	11.8

A. Natural Frequency

Initially, modal analysis was undertaken to determine the natural vibration characteristics of the PEM structure without any external forces. The purpose of the modal analysis is to determine the natural frequencies and the mode shapes and to extract the structural matrices which govern the modes and natural frequencies. The governing equation of the modal analysis is

$$M\ddot{u} + Ku = 0 \tag{1}$$

Where M is the structural mass matrix depend on density and matrix of shape functions, K is stiffness matrix, u and $\ddot{u}$ are nodal displacement vector and nodal acceleration vector respectively. The structural constraints were imposed on the four holes in the PCB board in all degrees of freedom. First ten natural frequencies of the modal analysis are listed in Table 2.

Table 2: First ten natural frequencies of the PEM structure

Frequency (Hz)	Mode Shape	Frequency (Hz)	Mode Shape
308.8		1251.8	
322.5		1345.2	
406.3		1383.8	
974.64		1502.6	
1230.7		2002.4	

B. Vibration Analysis

PEM structure spectrum analysis will determine the response of the structure under base excitation for a specific frequency. Spectrum analysis predicts the sustained dynamic response behavior of the structure, hence it viable to verify whether the design of the structure will withstand the resonance and harmful effects of forced vibration. The general equation of motion in the dynamic analysis is defined as

$$M\ddot{u} + C\dot{u} + Ku = F \tag{2}$$

Where M and K are as in Equation (1). C is the structural damping matrix and F is the applied load vector. For the PEM structure applied load vector is the model self-weight due to gravity as in Figure 3. Damping is assumed to be zero in this study. Obviously, without damping, Equation (2) becomes equation (1) with additional external force. The several numerical methods for solving the dynamic equation (Equation (2)) exists in the literature. Newmark time integration algorithm (see Linfield et al [10]) which is one of the widely used time integration algorithms, was used for the solution of Equation (2). The PEM structure base clamping holes were excited in a vertical direction. The excitation length (spectrum value) was kept as 5cm for all 10 natural frequencies (listed in Table (2)) in the modal analysis. The base excitation value 5cm is based on the typical road surface roughness.
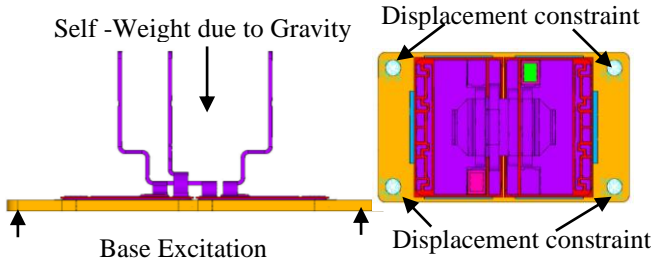

Figure 3. Self-weight due to gravity and base excitation location, and displacement constraint on the location on the model

For displacement excitation of the base, the displacement vector for each mode frequency is computed from mode coefficient and normalized eigenvector.

$$r_i = A_i\{\phi_i\} \tag{3}$$

where A_i mode coefficient and $\{\phi_i\}$ is the normalized eigenvector at the ith mode frequency. The normalised eigenvector $\{\phi_i\}$ is computed as $\{\phi_i\}^T[M]\{\phi_i\} = 1$. Mode coefficient A_i is defined as

$$A_i = S_i\gamma_i \tag{4}$$

Where, S_i is the spectral displacement vector for the ith mode (the displacement response spectrum at i^{th} natural frequency f_i from modal analysis) and γ_i is the participation factor for the ith mode defined as

$$\gamma_i = \{\phi_i\}^T[M][T]\{e\} \tag{5}$$

Where *[M]* is the structural mass matrix. *{e}* is six possible unit vectors corresponding to excitation (either displacement or rotation in x, y, z directions), and

$$[T] = \begin{bmatrix} 1 & 0 & 0 & 0 & (Z-Z_0) & -(Y-Y_0) \\ 0 & 1 & 0 & -(Z-Z_0) & 0 & (X-X_0) \\ 0 & 0 & 1 & (Y-Y_0) & -(X-X_0) & 0 \\ 0 & 0 & 0 & 1 & 0 & 0 \\ 0 & 0 & 0 & 0 & 1 & 0 \\ 0 & 0 & 0 & 0 & 0 & 1 \end{bmatrix} \tag{6}$$

X, Y, Z are global Cartesian coordinates of the nodes on the geometry, and X_0, Y_0, Z_0 are global Cartesian reference coordinates about which rotations are done. Ten resonant (natural) frequencies were obtained from the modal analysis and at those resonant frequencies base excitation, spectral analysis was embarked.
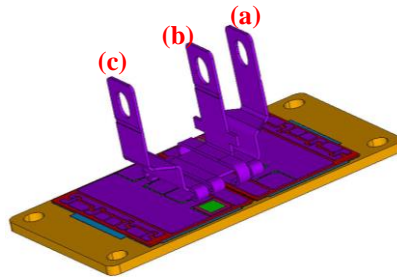

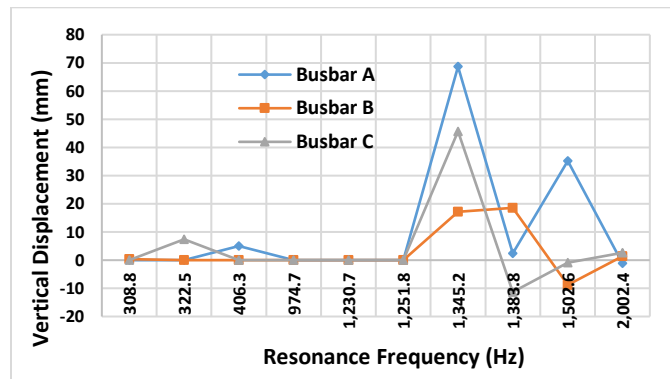Figure 4: The node labelling on the busbars

Figure 5: Vertical displacement of top nodes of the busbars against 10 resonant frequencies of the PEM structure
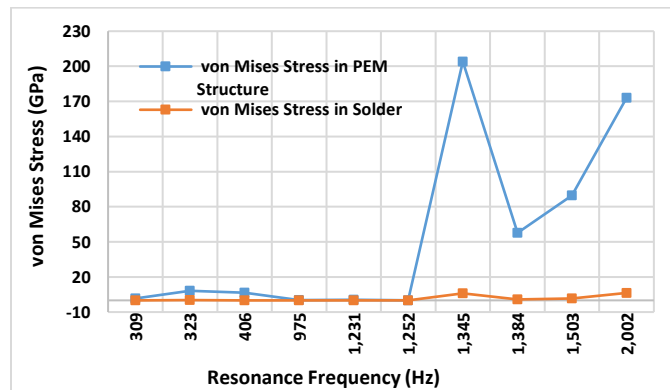

Figure 6: Maximum von Mises stress (GPa) in the PEM structure and solder layer.

The plots in Figure 5 illustrate the vertical displacement (mm) of the nodes on top of the busbars labelled as in Figure 4 against the 10 resonant frequency values in Hz. The peak displacements (response amplitude is maximum) of the busbars were observed near the three resonance frequencies 1345 Hz, 1384 Hz, 1503 Hz, hence higher stresses on the structure at these frequencies. Similarly, Figure *6* depicts the maximum von Mises stresses on the PEM structure as well as on the solder layer against the 10 resonant

frequencies values. Extreme von Mises stresses (as in Figure 7) on the structure were observed when excitation frequency reaches to 1345Hz.

.116E+08   .530E+11   .106E+12   .159E+12   .212E+12
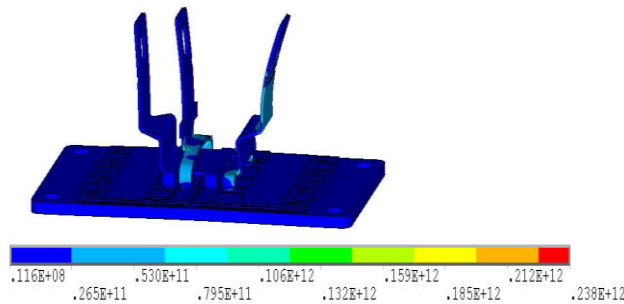.265E+11   .795E+11   .132E+12   .185E+12   .238E+12

Figure 7: von Mises stress distribution on the structure when the base excitation frequency reaches 1345Hz

III. COMBINED FATIGUE OF BASE EXCITATION VIBRATION AND THERMO-MECHANICAL CYCLING

Base excitation vibration causes fatigue in solder interconnect in high cycle regime such as resonant frequency. Solder interconnect undergo high cycle fatigue when mechanical stress repetition exceeds more than 10^4 cycles (see Eckert et al [11]). With the assumption of high cycle fatigue (HCF) occurs with low stresses in the elastic regime of a material, Basquin [12] proposed a stress based fatigue relations that connect the stress with number of cycles to failure. Another approach is based on Coffin-Manson-Basquin fatigue model

$$\frac{\Delta\varepsilon_{tot}}{2} = \sigma_f(2N_V)^b + \varepsilon_f(2N_V)^c \tag{7}$$

Where N_V denotes the vibration induced cycles to failure, σ_f is the fatigue strength coefficient, b is the fatigue strength exponent, ε_f is the fatigue ductility coefficient, and c is fatigue ductility exponent. The term $\Delta\varepsilon_{tot}$ is the total strain range for the particular frequency which can be extracted by spectral analysis. For Sn3.5Ag solder material, in the context of vibration related fatigue failure, the coefficients σ_f, b, ε_f, c of the Coffin-Manson-Basquin fatigue model were experimentally derived as 0.00045, -0.01, 62.93, and -0.66 respectively, see Eckert at al [11]. For known $\Delta\varepsilon_{tot}$ value, evaluating the lifetime N_V of equation (7) is not feasible analytically, hence a Newton Raphson type numerical approach can be utilized. In order to analyse the combined effect of base excitation vibration and thermo-mechanical cyclic loading induced fatigue on the reliability of the solder interconnect, spectrum analysis and thermal-structural analysis were undertaken. At the critical frequency of 1345 Hz, the total strain distribution in the solder interconnects was extracted. From the total strain distribution by base excitation vibration, lifetimes of the solder interconnects by vibration were derived by utilizing the Coffin-Manson-Basquin fatigue model (Equation (7)

In the thermo-mechanical analysis, the model will endure temperature cyclic loading. It was reported that for complex IC circuits the ambient operating temperature range for the extremely harsh environment such as electric car engine compartment was defined as -40° C to 125°C, see Johnson et al [13]. Hence the temperature load profile is ramped cyclic loading between -40° C to 125°C. According to MIL-STD-883E [14], the ramping time from hot to cold or cold to hot should not exceed one minute and the dwell time should not be less than 10 minutes, hence ramp time and dwell time of the thermal cycle were assumed as 1 and 10 minutes respectively. Moreover, three-point displacement boundary restrictions were imposed on the model. A unified creep and plasticity strain (inelastic) constitutive equation was utilised to evaluate the inelastic strain in solder interconnect. Anand constitutive equation for inelastic (viscoplastic) strain rate is defined as in equation

$$\dot{\varepsilon}_{Visco} = Ae^{\frac{-Q}{RT}}\left[\sinh\left(\xi\frac{\sigma}{s}\right)\right]^{(1/m)} \tag{8}$$

The values of the Anand model (Equation (8)) parameters were listed in Table 3.

Table 3: The values of Anand model coefficients for equation (5)

Anand Parameters	Value
A (sec^{-1})	2.23 (10^4)
Q/R (° k)	8900
ξ	6
m	0.182
$\hat{s}$ (MPa)	73.81
n	0.018
h_0 (MPa)	3321.15
a	1.82
s_0 (MPa)	39.09

For low cycle fatigue, Coffin-Manson fatigue life model is widely used

$$\Delta\varepsilon_{in}(N_{TM})^k = C \tag{9}$$

Where $\Delta\varepsilon_{in}$ is the accumulated equivalent inelastic strain during a stabilised cycle, N_{TM} is fatigue life by thermo-mechanical failure, k is fatigue ductility exponent and C is the fatigue ductility coefficient. For low cycle fatigue, the values of the coefficients of Sn3.5Ag solder material C and k are respectively 3.64 and 0.76, see Kanchanomai et al [15]. In order to preclude the mesh dependency of the damage indicator $(\Delta\varepsilon_{in})$, volume weighted averaging (VWA) method is widely applied.
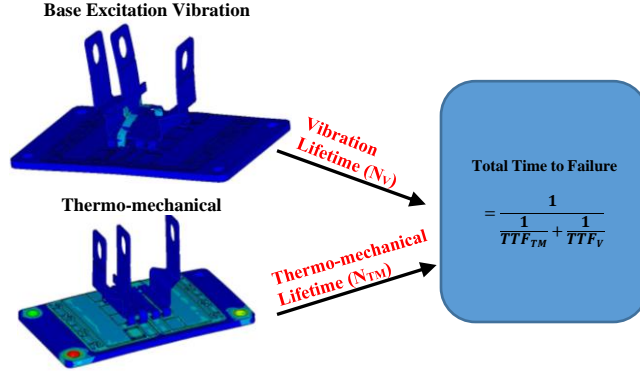

Figure 8: Illustration of the total lifetime of solder interconnect by low cycle fatigue (thermo-mechanical) and high cycle fatigue (vibration)

The PEM structure consists of four solder interconnect layers. The solder interconnect sandwiched between the silicon chip and copper layer is labelled as 'solder layer 1' and 'solder layer 3'. Solder layer 1 is adjacent to the busbar C (see Figure 4). The solder layer 3 is nearby to busbar a. The solder interconnects sandwiched between the copper foil and PCB board are labelled as 'solder layer 2' and 'solder layer 4'. The 'solder layer 2' is closer to the busbar c and 'solder layer 4' is adjacent to busbar a. Table 4 exhibit the total lifetime of each solder interconnect by combining the high cycle (Vibration induced failure) fatigue model and low cycle (thermo-mechanical failure) fatigue model. Generally, solder interconnect sandwiched between chip and the copper layer relatively higher lifetime, in contrast, the solder interconnect between the copper layer and PCB board lower lifetime specifically, the layer adjacent to busbar c.

Table 4: Lifetime of the solder interconnect layers

Solder Layer Numbering	1	2	3	4
Number of Cycles to Failure (N_V) by Vibration	353202	587507	344651	586178
Time (s) to Failure by Vibration	262.2	436.8	256.2	435.8
Number of Cycles to Failure (N_{TM}) by Thermo-mechanical Fatigue	1230	4714	1255	4716
Time (s) to Failure by Thermo-mechanical Fatigue	1623936	6222283	1656227	6225151

Two total damage prediction approaches combining the vibration induced damage and the thermo-mechanical damage are in the in the industry standards. A relatively simple approach is the Miners rule approach (Linear damage superposition approach (LDSA)) which is referred to in the standards IPC-SM-785 and IEEE141.3. Another approach is the incremental damage superposition method (IDSA) which is mentioned in standard IEEE141.3, see the Qi et al [16]. In this study, LDSA is utilized. In LDSA, total damage rate (D_{Total}) is defined as

$$D_{Total} = \frac{1}{TTF} = \frac{1}{TTF_V + TTF_{TM}} \tag{10}$$

Where TTF_V, and TTF_{TM} are time to failure by vibration and thermo-mechanical fatigue respectively. TTF_V and TTF_{TM} were evaluated and then using Miners rule total lifetime (N_T) by combined failure were derived as in Figure 8. Vibration induced failure is much severe at the extreme resonant frequency of 1345 Hz, in contrast, thermo-mechanical failure is slow progress. Hence vibration induced failure at the resonant frequency is more dominant and severe than thermo-mechanical failure. Solder interconnects between chip and copper trace are more prone to failure by both failure mechanisms compared to the solder interconnect between PCB and copper trace.

IV. VEHICLE DYNAMICS

Interaction between wheels and the road surface causes a dynamic excitation in the engine compartment due to the dynamic properties of the vehicle's suspension system, and speed of the vehicle in an EV.

A. Road Profiles

ISO 8608 [17] standardize the classification of the road surface profiles based on a comparison of the measured Power Spectral Density (PSF) values. According to ISO 8608, typically there are eight categories of the road surfaces labelled from A to H. Profile

H has a high degree of surface roughness which implies that that road is very poor. With artificial road roughness classification *k*, road surface roughness profile *h(x)* can be regenerated as described in [18]

$$h(x) = \sum_{i=1}^{N} \sqrt{\Delta n} \cdot 2^k \cdot 10^{-3} \left(\frac{n_o}{i.n}\right) Cos(2\pi.i.\Delta n.x + \varphi_i) \tag{11}$$

where $x \in [0, L]$, is the abscissa variable within the total length of the road *L*. *k* is the road roughness classification value from ISO road profile classification and it assumes an integer between 3 and 9. n_0 is the number of cycles per meter sampled (typically 0.1 cycles/m, see Agostinacchio et al [19]). The variable φi denotes a random phase angle drawn from a uniform distribution within the range of π and $-\pi$. Δn is the frequency at which the road profile is sampled uniformly over its entire length *(Δn =1/L)*. *n* is the spacial frequency with $N = \frac{n}{\Delta n}$.

B. Quarter Car Suspension Model

The widely used simple Quarter Car Model (QCM) can reasonably estimate the dynamic interaction between the vehicle and road roughness profile. QCM can approximate the vertical vibrations of a car and hence vibration of the PEM device inside the car in the engine compartment can be approximated. QCM consists of two body system (sprung and unsprung mass) with two springs and damper to represent the suspension and elasticity of the wheel as in Figure 9
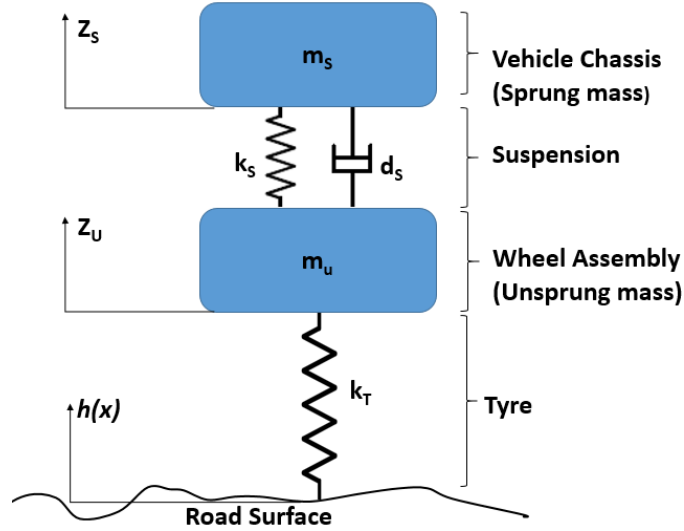

Figure 9: Schematic of the Quarter Car Model

The mathematical model of the QCM passive suspension system is described as

$$m_S \frac{\partial^2 Z_S}{\partial t^2} + d_S \left(\frac{\partial Z_S}{\partial t} - \frac{\partial Z_U}{\partial t}\right) + k_S(Z_S - Z_U) = 0 \tag{12}$$

$$m_U \frac{\partial^2 Z_U}{\partial t^2} - d_S \left(\frac{\partial Z_S}{\partial t} - \frac{\partial Z_U}{\partial t}\right) - k_S(Z_S - Z_u) + k_T(Z_u - h(x)) = 0 \tag{13}$$

Where Z_U and Z_S are vertical displacements of suspension and body. m_S represent the car chassis mass and m_U denotes car wheel assembly mass. The suspension stiffness k_S, tyre stiffness k_T, and suspension damping c_S are extracted from [19] for various vehicle types and listed in Table 5. The dynamic equations (Equations (12) and (13)) of the QCM can be stated in the standard-state variable form [19] and defined as

$$\frac{\partial}{\partial t}\begin{bmatrix} Z_U - h(t) \\ \frac{\partial Z_U}{\partial t} \\ Z_S - Z_U \\ \frac{\partial Z_S}{\partial t} \end{bmatrix} = \begin{bmatrix} 0 & 1 & 0 & 0 \\ -\frac{k_U}{m_U} & \frac{d_S}{m_U} & \frac{k_S}{m_U} & \frac{d_S}{m_U} \\ 0 & -1 & 0 & 1 \\ 0 & \frac{d_S}{m_S} & -\frac{k_S}{m_S} & -\frac{d_S}{m_S} \end{bmatrix} \begin{bmatrix} Z_U - h(t) \\ \frac{\partial Z_U}{\partial t} \\ Z_S - Z_U \\ \frac{\partial Z_S}{\partial t} \end{bmatrix} \tag{14}$$

Standard variable form (Equation (14)) can be solved numerically, and from the numerical solution, the vertical displacement of the car chassis (suspension deflection) on which PEM device is mounted, can be approximated for a particular road profile.-

Table 5. Vehicle parameter values [19]

Parameters	Unit	Car	Bus	Truck
Sprung mass m_S	[kg]	400	4000	4500
Unsprung mass m_U	[kg]	40	550	650
Suspension stiffness k_S	[N/m]	21000	320000	570000

Suspension damping d_S	[N.s/m]	1500	10000	21000
Tyre stiffness k_T	[N/m]	150000	1700000	3000000

Figure *10* illustrates the vertical road profile and the subsequent suspension deflection of the severe road profile *(K)*. The suspension defelection is for the car parameters in the model (Equations (13) and (14). *Figure 11* exhibit the location of the PEM device on the car chassis.
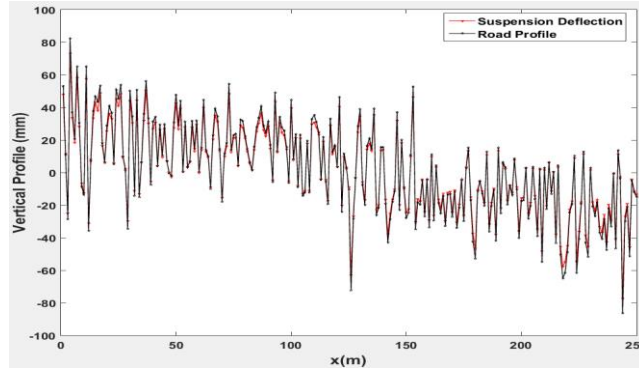

Figure 10: Road vertical profile (mm) and suspension vertical deflection (mm) along the 250m length of the road for severe road condition (k =9)
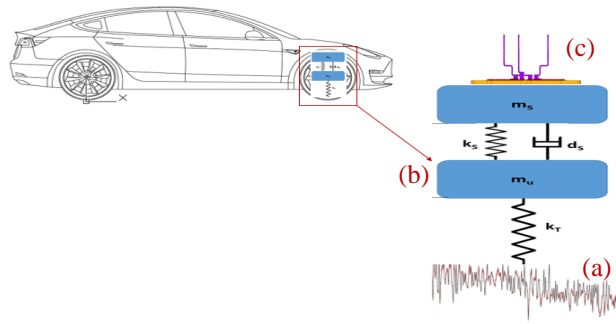

Figure 11: (a) Severe road vertical profile as in Figure 10, (b) QCM suspension system under the car chassis, (c) PEM device without encapsulation on the engine compartment.

C. Transient Vibration Analysis

The governing physics of transient dynamic analysis is as in Equation (2). Assuming an EV is travelling in 30Km/h, then for every 0.12s, the vehicle will travel for every meter of the road. The road profile is as in Figure *10* where tyre displacement and subsequent suspension displacements are plotted. Typical car engine compartment temperature at the close proximity to the engine is 120°C, Temperature at the remote location from the engine is 105°C, see Myers [20]. Hence typical environment temperature of the PEM device within the car engine compartment was assumed as 105°C. Hence a numerical transient finite element analysis (FEA) with vertical movement as in suspension deflection was simulated (PEM device was on top of the suspension). The environment temperature (105 °C) of the car compartment was set as a reference temperature in the FEA simulation.
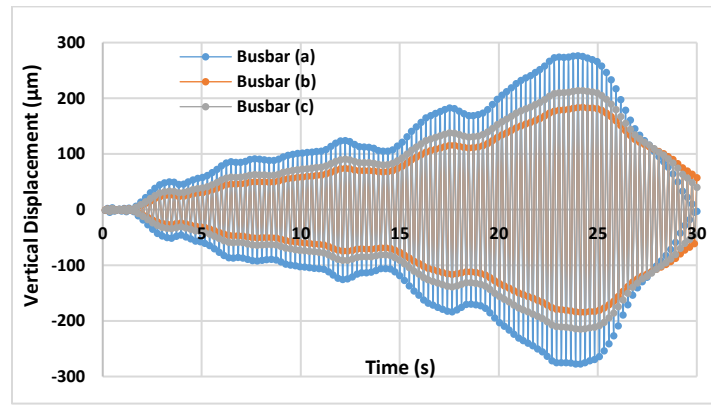
Figure 12: Vertical displacement related to suspension deflection of the nodes on top of the busbars.
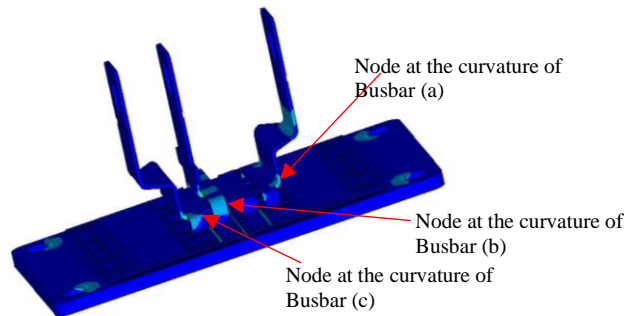

Figure 13: Location of corner nodes where extreme von Mises stress distribution observed at the busbars
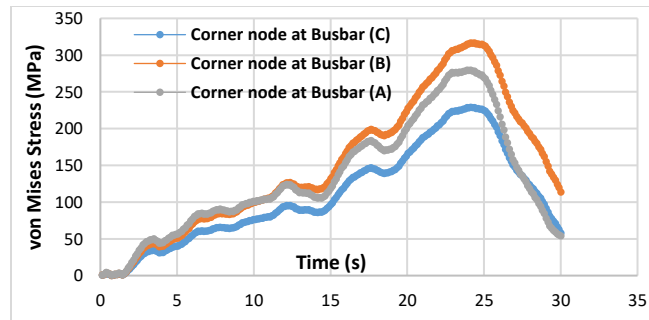

Figure 14: von Mises stress (MPa) at the curved part of the busbars as in Figure 13.

From Figure *13* and Figure *14*, it can be concluded that as time progresses the stresses on the busbar increases and subsequently other failures such as interconnect failures can prop up. In essence, if the EV travels on a bumpy road, increased distance and the speed of the vehicle will increase the possibility of the fatigue related damage on the PEM module.

V. MODEL ORDER REDUCTION IN VIBRATION ANALYSIS

Since the system arising from vibration analysis is a second order system as in Equation (2). In PEM device vibration finite element modelling, the dimension of the resulting dynamical system is equal to the number of nodes (element nodes) in the discretized model multiplied by the number of degrees of freedom. Hence model order reduction (MOR) is sought in order to reduce the system dimension and the reduction in computational complexity. An essential feature of MOR techniques is their simplification of large physical systems to a smaller system. The simplification of the system introduces an error however this error value should be within an acceptable limit for the methods. The transformation of the full order system into a reduced order system has been accomplished by various mathematical approaches. Fundamentals methods in the area of MOR were first published in the 1980s and 90s. The MOR techniques can be categorised into two main groups namely projection based moment matching techniques and singular value decomposition (SVD) or Gramian based method. When an SVD based method is applied to stable systems, it preserves the stability of the system and additionally estimates a priori bound of the approximation error. However, for large systems, the SVD based MOR techniques are computationally expensive to implement. Moment matching or Krylov subspace methods are based on matching a certain number of moments. Compared to SVD based methods, moment matching methods are easier to implement numerically, however, moment matching methods do not have a priori error bound, hence, this is a disadvantage as the error can become larger than the allowable errors. Therefore the moment matching MOR methods were sought.

The second order system of the general equation of the motion (Equation (2)) can be transformed into a linear system (see Chahlaoui et al [21]) by introducing ξ

$$\xi = [u^T, \ (\dot{u})^T]^T \tag{15}$$

Where the transformed linear system is defined as

$$\begin{bmatrix} I & 0 \\ 0 & M \end{bmatrix} \dot{\xi} = \begin{bmatrix} 0 & I \\ -K & -C \end{bmatrix} \xi + \begin{bmatrix} 0 \\ F \end{bmatrix} \tag{16}$$

Since mass matrix M is invertible, hence Equation (16) can be defined in simplified from

$$\dot{\xi} = A\xi + B \tag{17}$$

Where $A = \begin{bmatrix} 0 & I \\ -M^{-1}K & -M^{-1}C \end{bmatrix}, B = \begin{bmatrix} 0 \\ M^{-1}F \end{bmatrix}$

Laplace transform of the Equation (17) yields

$$s\xi(s) = A\xi(s) + B(s) \tag{18}$$

The transfer function *H(s)* is defined as

$$H(s) = (sI - A)^{-1}B = -\sum_{i=0}^{\infty} m_i s^i, \tag{19}$$

where $m_i = A^{-i}(A^{-1}B)$ is the ith moment of transfer function H. The stiffness ($K \in \mathcal{R}^{n \times n}$), damping ($C \in \mathcal{R}^{n \times n}$) and mass ($M \in \mathcal{R}^{n \times n}$) matrices can be extracted from ANSYS finite element code as described by Rudnyi et al [22]. The resulting compact system of the PEM device structure (Figure *2*) is large, hence moment matching based MOR were utilised. In essence, the moment matching based MOR technique involves choosing the transformation matrix *V* and projection matrix *W* in order to transform the compact system into lower dimensional reduced system approximation.

$$\dot{z} = W^T A V z + W^T B(t) = A_r z + B_r \tag{20}$$

where $(W, V) \in \mathcal{R}^{n \times m}, m \ll n$. The residual error *r* caused by the MOR is defined as $r = A\xi + B(t) - \dot{\xi}$, and requirement of the inner product of *r* with *W* should be zero ($W^T r = 0$). If *W = V*, then the MOR is named orthogonal projection methods and solution of Equation (2) is generated from the reduced model by following substitution, $\xi \approx Vz$.

The most popular moment matching based MOR schemes are based on Krylov subspaces. One of the drawbacks of the moment matching based MOR is it requires prior knowledge of the number of moments to be matched and the expansion point for the transfer function, see Feng et al [23]. I.e. the dimension of the reduced system should be known priory before applying the MOR to full compact system. Expansion point (*s*) depend on the frequency (*f*) of the linear time invariant system ($s = 2\pi j f$). In most cases the, expansion point is chosen as zero. Various adaptive schemes of moment based MOR were in the literature. In this study, the expansion point was assumed as zero and the dimension of the reduced order system is iteratively chosen for a given tolerance value. Iteration starts with user input of maximum acceptable dimension (*r_{max}*) of reduced order system as well as with the user given permissible tolerance value. Then the project matrices *V* and *W* are computed by a MOR method with user defined minimum dimension and the error (ε) is computed such that

$$\varepsilon = \frac{\|H(s) - H_r(s)\|}{\|H(s)\|} \tag{21}$$

where *H(s)* and *H_r(s)* are transfer function (Equation (19)) of full and reduced systems. The iteration starts with one column vector of the projection matrices *V*, *W* and until error value ε is less than the acceptable error value, it adds one column of the projection matrices at each iteration. If the number of columns of the projection matrices exceeds the permissible number of dimension (*r_{max}*) of the reduced order system, iteration stops.

The widely used Krylov subspace based method Passive Reduced order Interconnect Macromodeling Algorithm (PRIMA) which was originally developed for the RLC circuit system by Odabasioglu et al[24]. Although more expensive in computational cost in forming the projection matrix *V* of the PRIMA method in comparison with other Krylov based method, PRIMA is more accurate, and it preserves the stability and passivity of the reduced system. The Arnoldi MOR algorithm (AA) finds the orthogonal vectors of the projector matrices as the columns for projection matrices of Krylov subspaces. This report utilizes the Arnoldi MOR based on the algorithm of Chu et al [25]. In Arnoldi algorithm, the projection matrix *V* is an orthogonal matrix, such that $V^T V = I$. Lanczos MOR algorithm iteratively applies a modified version of Gram Scmidt process to form two pairs of biorthogonal basis matrices for the Krylov subspace, *V* and *W*. In this study, the Lanczos algorithm by Binion and Chen [26] was utilised adaptively in order to obtain the reduced system with optimum order for a user given tolerance value. If the user set tolerance is not viable during the iteration, then the adaptive code output the least error and the associated projection matrices with the best order.

Since the limitation with the computing resources, a subsection of the PEM structure device was analysed in the Ansys finite element code for MOR application as in Figure *15*. The subsection section consists of aluminum trace, chip, solder, copper, dielectric solder and PCB. The order of the full compact system (Equation (10)) is 1132. Three MOR algorithms (PRIMA, Global Arnoldi, Lanczos) were implemented in MatLab and applied to the full compact transient system extracted from Ansys finite element code. The resulting least error (Equation (21)) and the associated order of the reduced system by MOR are listed in Table *6*.
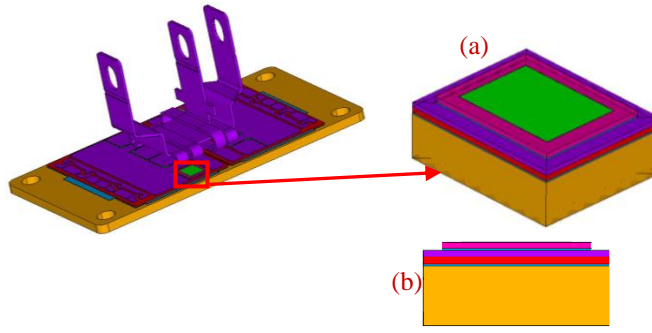
Figure 15: (a) Subsection of the PEM structure for MOR analysis, (b) Side view of the subsection.

Table 6: The least error and the resulting order of the reduced system by various MOR algorithms

MOR Algorithm	Least Error	Order of the reduced system
PRIMA [24]	3.741×10^{-13}	6
Arnoldi [25]	1.189×10^{-12}	8
Lanczos [26]	1.359e-06	4

Since compact system (Equation (17)) consists of a pair of blocks row and column wise, the order of the reduced block matrix system should be in even number. PRIMA MOR performs better in this example compared to the other two methods. A finite difference discretization can be applied to solve the time invariant system (Figure *15*) at a time step Δt.

$$\xi(t + \Delta t) = (A\Delta t + I)\xi(t) + B\Delta t \qquad (22)$$

The order of the computational complexity of the matrix vector multiplication for the full compact system (Equation (22)) is $O(1132^2)$. Furthermore, the order of the complexity of the reduced system derived by PRIMA MOR is $O(6^2)$. In the desktop with Intel Xeon 2.40GHz processor, typical time consumed for one iteration of the full compact system (Equation (22)) is 48 ms, while typical time consumed for one iteration of the reduced system is 0.91 ms.

VI. CONCLUSION

The study focused on finite element modelling and analysis of base excitation vibration of an IGBT power electronic module structure. The PEM structure without the molding compound was utilised in order to estimate the worst case scenario. To simplify the modelling and reduce the computational cost, the wirebonds on the PEM structure were also omitted in the model. PEM structure with many wirebonds is difficult to model due to limited academic computing resources. Initially, ten natural frequencies were extracted. From the natural frequencies, the critical resonant frequency was identified for gravitational self-load of the structure. The vertical base excitation was applied on four corner clamping points. The stress and strain range for 0.05m vertical displacement base excitation at the critical resonant frequency was identified which is 1345 Hz for the PEM structure.

The concurrent effect of vibration induced fatigue and thermo-mechanical fatigue on the reliability of the solder interconnect was estimated by using linear damage superposition approach (LDSA). The total damage by the combined mode of vibration and thermo-mechanical fatigue was estimated for four solder interconnects. It can be concluded that the vibration induced damage is more dominant than thermo-mechanical fatigue induced damage. Furthermore, solder interconnect sandwiched between chip and the copper layer has higher damage, in contrast, the solder interconnect between the copper layer and PCB board.

PEM in an EV engine compartment undergoes significant dynamic excitation due to dynamic properties of the suspension system, speed of the vehicle and more dominantly the surface roughness of the road. Well known simple quarter car model (QCM) can reasonably estimate the PEM structure excitation in the engine compartment for a known the road surface roughness profile. For a severe road roughness profile from the ISO 8608 standard, QCM generated a dynamic excitation of the suspension system, and this suspension excitation load was applied to a PEM structure to mimic the vehicle dynamic excitation. For a vehicle speed of 30 km/h, the stress strain distributions of the PEM structure was extracted. It can be concluded that as the time progresses the accumulation of stresses on the structure increases for a severe road surface profile which eventually lead to failure of the structure.

Modelling vibration of PEM structure involves the second order dynamical system. System dimension is equal to the number of nodes multiplied by the number of degrees of freedom. Obliviously for the large structure like PEM device, finite element modelling requires a large number of elements discretisation. In order to speed up the computational process, model order reduction (MOR) is sought. The second order system is transformed into a first order coupled system and then MOR was applied. Due to limitation with academic computing resources, a submodel was utilized. The submodel consists of the part of the PEM structure as in Figure *15*. Three MOR techniques such as PRIMA, Arnoldi, Lanczos algorithms were utilized for the subsystem discretization. It can be concluded that PRIMA outperforms better than other methods. Computational time ratio between PRIMA reduced system iteration and the full system iteration is 1:53.

REFERENCES

[1] W. W. Sheng and R. P. Colino, Power electronic modules, CRC Press, 2009

[2] C. Durand, M. Klingler, D. Coutellier, and H. Naceur, Power cycling reliability of power module: a survey, IEEE Transactions on device and materials reliability, 16, 2016, pp 80-97

[3] Dave Steinberg, Vibration analysis for electronic equipment, John Wiley & Sons, 2000

[4] J. Gu, D. Barker, and M. Pecht, "Prognostics implementation of electronics under vibration loading," Microelectron. Reliab., vol. 47, no. 12, pp. 1849–1856, 2007

[5] Tae-Yonk Park, Jong-Chan Park, Hyun-Ung Oh, Evaluation of structural design methodologies for predicting mechanical reliability of solder joint of BGA and TSSSOP under launch of random vibration, International journal of fatigue, 114, 2018, pp 206 – 216

[6] Hu Jiaxing, Jing Bo, Sheng Zengjin, Lu Fang, Chen Yaojun, Zhang Yulin, Failure and failure characterization of QFP package interconnect structure under random vibration condition, Microelectronic reliability, 91(1), 2018, pp 120-127

[7] Fang Liu, Ye Lu, Zhen Wang, Zhiming Zhang, Numerical simulation and fatigue life estimation of BGA packages under random vibration loading, Microelectronic reliability, 55 (12), 2015, pp 2777 – 2785

[8] Tong An, Chao Fang, Fei Qin, Huaicheng Li, Tao Tang, Pei Chen, Failure study of Sn37Pb solder joints using temperature cycling, random vibration and combined temperature cycling and random vibration tests, Microelectronic reliability, 91 (2), 2018, pp 213 – 226

[9] G. Mitic, H. P. Desischer, G. Lefranc, T. Licht, AlSiC composite materials in IGBT power modules, 35th IEEE Industry Applications conference and World conference on industrial applications of electrical energy, Rome, Italy, Oct 2000

[10] George Lindfield, John Penny, Numerical methods, 4th edition, Academic press, 2019

[11] Tilman Eckert, Wolfgang H. Müller, Nils F. Nissen, and Herbert Reichl, A Solder Joint Fatigue Life Model for Combined Vibration and Temperature Environments, 59th Electronic Components and Technology Conference (ECTC), San Diego, USA, May 2009

[12] O. H. Basquin, The Exponential Law of Endurance Tests, American Society for Testing and Materials Proceedings, Vol. 10, 1910, pp. 625-630

[13] R. Wayne Johnson, John L. Evans, Peter Jacobsen, James R. Thompson, Mark Christopher, The changing automotive environment: High temperature electronics, IEEE Transactions on electronics packaging manufacturing, 27 (3), July 2004.

[14] MIL-STD-883E, Test method standard microcircuits, department of defense, USA, 1996

[15] Chaosuan Kanchanomai, Yukio Miyashita, and Yoshiharu Mutoh, Low-cycle fatigue behavior and mechanisms of a lead-free solder 96.5Sn/3.5Ag, Journal of electronic materials, 31 (2), 2002

[16] Haiyu Qi, Michael Osterman, Michael Pecht, Modelling of combined temperature cycling and vibration loading on PBGA solder joints using an incremental damage superposition approach, IEEE Transaction on advanced packaging, vol 31, No 3, Aug 2008.

[17] ISO 8608 (1995) Mechanical vibration, road surface profiles. Reporting of measured data.

[18] Ding-Geng Chen, Yuhlong Lio, Hon Keung Tony Ng, Tzong-Ru Tsai, Statistical modelling for degradation data, Springer, 2017

[19] M. Agostinacchio, D. Ciampa and S. Olita, The vibrations induced by surface irregularities in road pavements- a Matlab approach, European Transport Research Review, 6, 2014, pp 267 – 275

[20] Bruce. A. Myers, Cooling issues for automotive electronics, Automotive Electronics, Electronic Cooling, 9 (3), 2003

[21] Younes Chahlaoui, Kyle A. Gallivan, Antoine Vandendorpe, Paul Van Dooren, Model reduction of second order systems. In: Benner P., Sorensen D.C., Mehrmann V. (eds) Dimension Reduction of Large-Scale Systems. Lecture Notes in Computational Science and Engineering, vol 45. Springer, Berlin, Heidelberg, 2005

[22] E. B. Rudnyi and J. G. Korvink, Model order reduction for large scale engineering models developed in Ansys, In: J. Dongarra, and K. Madson, Applied parallel computing: state of the art in scientific computing, Springer, 2006

[23] Lihong Feng, Jan G. Korvink, Peter Benner, A fully adaptive scheme for model order reduction based on moment matching, IEEE Transactions on component and packaging and manufacturing technology, 5 (12), 2015

[24] Altan Odabasioglu, Mustafa Celik, and Lawrence T. Pileggi, PRIMA: Passive reduced-order interconnect macromodeling algorithm, IEEE Transactions on computer-aided design of integrated circuits and systems, 17 (8), Aug 1998, pp 645 - 654

[25] Chia-Chi Chu, Ming-Mong Lai, Wu-Shiung Feng, Model-order reductions for MIMO systems using global Krylov subspace methods, Mathematics and computers in simulation, 79, 2008, pp 1153 – 1164

[26] David Binion, Xiaolin Chen, Coupled electrothermal-mechanical analysis for MEMS via model order reduction, Finite elements in analysis and design, 46, 2010, pp 1068 -1076